# Tidal and Solar Radiation Impacts near the Tiwi Islands in the Southern Arafura Sea

**R. Robertson[1], C. Zhao[2], W. Wang[2], Z. Xu[2], Z. Liu[3], and P. S. Hartlipp[4]**

[1]China-Asean College of Marine Science, Xiamen University Malaysia, Sepang, Malaysia.

[2]CAS Key Laboratory of Ocean Circulation and Waves, Institute of Oceanology, Chinese Academy of Sciences Qingdao, China.

[3]State Key Laboratory of Marine Environmental Science, and Department of Physical Oceanography, College of Ocean and Earth Sciences, Xiamen University, Xiamen, China.

[4]University of New South Wales Canberra, Canberra, ACT, Australia

30 August 2021

Corresponding author: Robin Robertson (Robin.Robertson@xmu.edu.my) (Orchid ID: 0000-0002-1855-8411)

**For Submission to *Journal of Geophysical Research: Oceans***

**Key Words:** tides, internal tides, solar radiation

**Key Points:**

- Topographic location is key to whether the tidal flow is barotropic or baroclinic near the Tiwi Islands
- Tidal advection dominates in the shallow waters west of the Tiwi Islands; however, on the east side internal tides were present
- With a stratified water column in coastal waters, high fluorescence is trapped in the lower layer

## Abstract

Time series of shipboard observations in the southern Arafura Sea near the Tiwi Islands indicated that the water column dynamics differed between the east and west sides of the islands. On the west side, the water column, characterized by temperature, salinity, and velocity, was barotropic and tidal advection dominated. On the east side, the water column was baroclinic and internal tides were present along with tidal advection. These conditions affected the distribution of the turbidity and fluorescence in the water column. Likewise, the influence of the daily solar radiation cycle reached the bottom on the western side, but was limited to the upper layer above the thermocline on the eastern side. The fluorescence peaks also differed between the east and west sides, with the eastern side dominated by the semidiurnal tides and the western side by the daily solar cycle. Fluorescence integrated over the water column was much higher on the eastern side than the western side. Also on the eastern side, fluorescence was limited to the lower layer, while on the western side, it encompassed the entire water column at times and peaked below the warmer, higher oxygenated water generated by solar radiation and surface mixing. These dynamics have distinct implications for biological productivity and also may affect a proposed tidal power system in the region.


## 1 Introduction

Ocean dynamics are important in coastal waters for many reasons, replenishment of nutrients, tidal power, detection of harmful algal blooms (HAB), dilution of pollutants, and the distribution of heat and river outflow. These impact water quality, biological productivity, and fishing stocks [*Moore et al*., 2019]. The region north of Australia, particularly the central section near Darwin and the Tiwi Islands, is an area of the world least impacted by humans [*Halpern*, 2008].

Generally, the primary processes involved in ocean circulation and mixing are: major geostrophic currents, coastal currents, wind, tides, eddies, upwelling, and the daily solar radiation cycle. However, in the southern Arafura Sea near the Tiwi Islands and Darwin, there are no major geostrophic currents, strong coastal currents, or eddies [*Condie*, 2011; *Schiller*, 2011; *Kampf*, 2016]. A weak coastal current does flow from the Joseph Bonaparte Gulf north and then east around the Tiwi Islands [*Condie*, 2011]. However, the tides there are quite large [*Easton*, 1970] and the daily solar cycle is strong, due to its location. The tropical location, a little south of the doldrums and Intertropical Convergence Zone (ITZC), results in typically weak winds, although daily sea breezes and thunderstorms are common. These generally sluggish winds along with a feeble Coriolis parameter, reduce the strength of upwelling events. Consequently the potential forcing for the circulation and mixing is limited to primarily tides and the daily solar radiation cycle, with winds contributing in a minor way, mainly through surface mixing. In most observational data, many of these processes are active complicating the dynamics. These diminished role of many of the usual processes provides a unique opportunity to essentially investigate the role of tides and solar radiation nearly in isolation

Prior physical oceanographic studies in the Arafura Sea have primarily been modelling studies that covered a broad area [*Schiller*, 2011] or focused either on the Gulf of Carpentaria [*Condie*, 2011] or on the northern region [*Kampf*, 2016]. Only one observational study [*Moore et al.,* 2019] collected observations near our study area off the Tiwi Islands and their observations were primarily chemical and biological, taking and analyzing water samples. There are several moorings north of this region as part of the Integrated Marine Observing System

(IMOS), but they are further out on the continental shelf, with different dynamics. Two are relatively near our observation sites, DAR and LYN. Thus, there is a paucity of observational data for the region resulting in the conditions not being well-known and insufficient for model validation. The long-term transports in the Arafura Sea are dominated by the seasonal monsoons and the associated winds [*Condie*, 2011]. However, these studies point out that tides are a major factor for the region near the Tiwi Islands. There are no strong alongshore or on-offshore currents near the islands. They also indicated that wind-induced upwelling of nutrient-rich deeper waters and other mixing mechanisms are important factors for biological productivity in these oligotrophic waters [*Condie*, 2011].

Tides have several roles in the ocean dynamics in shallow water. First, they advect water on- and off-shore. Second, they generate tidal fronts by mixing the entire water column. Third, they induce mixing through shear instabilities. Fourth, they affect the available light for photosynthesis by shifting the depth of the thermocline. Fifth, they alternately entrain and deposit both phytoplankton and sediment through the alternating strength of the tidal velocities. Finally, they also advect biological species back and forth during the ebb and flood tidal cycle. Tides have been found to influence biological productivity and composition in other regions, such as San Francisco Bay and the North Sea, where strong tidal signals were present in biological productivity and species diversity [*Cloern*, 1991; *Blauw et al*., 2012;] The predominant mechanisms were 1) entrainment and sinking due to changes in the magnitude of the tidal currents (period of 6.2 hours, 2) advection of different waters during the tidal cycle (period of 12.4 hours), and 3) the day-night diurnal cycle (period of 24 hours). *Kampf* [2015] used a model to investigate plankton blooms due to upwelling in the Arafura Sea. He found little response near the Tiwi Islands; however, a strong response in the northwest Arafura Sea. Also using a model *Condie* [2011] determined the general flow was northeast off Melville Island, the largest of the Tiwi Islands and was not wind-driven, but driven by the general circulation. The flow and mixing in this region is not only important for resupply of nutrients and biological productivity, but also it is the proposed site of a tidal power station [*Tethys*, 2019].

In a joint voyage on the RV Investigator with an atmospheric science group studying Tropical Storm Hector, leg 2 of IN2019v06, we collected temperature, salinity, and velocity time series and observed the physical oceanographic conditions at three areas near the Tiwi Islands. Our observational program is described in Section 2 and a supporting modeling effort in Section 3. Section 4 gives our results outlining the different conditions on the east and west sides of the Tiwi Island. Finally a summary is provided in Section 5.

## 2 Observational Effort

Several times series of hydrographic and velocity profile data were collected from RV Investigator in the southern Arafura Sea near the Tiwi Islands off Northern Australia between November 12 and December 16, 2019 (Figure 1). The first time series was on the eastern side of the island with the remaining time series on the western side, one of which was in a trench off Melville Island (Figure 1). Multiple systems were used to collect data, including a Conductivity, Temperature, Depth (CTD) profiler, a shipboard Acoustic Doppler Current Profiler (SADCP), and the ship's Underway system.

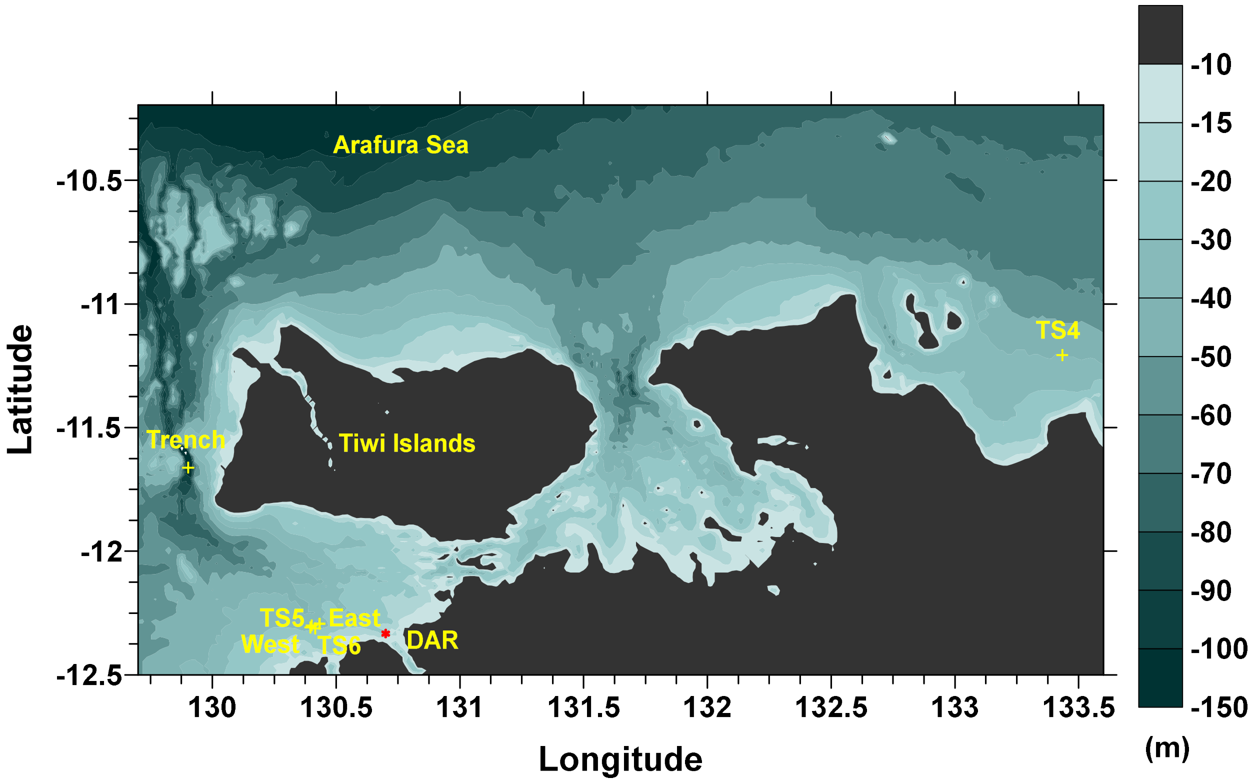


**Figure 1. The bathymetry of Arafura Sea around Tiwi Islands with the Time Series locations marked by yellow crosses and labeled TS4, TS5, and TS6, respectively. The locations of the casts on the east and west sides of Time Series 4 and 5 and the casts in the trench (TS8) are also indicated by yellow crosses and labeled. The red dot labeled DAR indicates the location of the IMOS Darwin mooring. The IMOS LYN mooring is located at Lynedoch Shoals, north of this area at 130° 20.94’ E, 9° 56.34’ S.**

## 2.1 CTD

Hydrographic profiles were collected using a Sea-Bird SBE911+ CTD attached to a 24-bottle Rosette system. Dual pumps, temperature, conductivity, and oxygen sensors and single transmissometer, nephelometer, Wetlabs ECO-chlorophyll, Wetlabs ECO-scattering, PAR, and altimeter sensors were installed on the CTD. Data was processed using the CSIRO Cappro software version 2.9 and binned at 1 dbar intervals. Temperature and salinity uncertainties were ±0.0015°C and ±0.005 psu, respectively.

## 2.2 Shipboard ADCP (SADCP)

The shipboard ADCP (SADCP) provided velocities for most of the water column in these shallow waters, depths <50 m, so a Lowered ADCP was not used. A RDI 150 kHz ADCP’s was operated nearly continuously from the RV Investigator in a broad beam model. It was set with 2 m bins and output data at ~5 minute intervals, with the exception of the first 2 days when the bin size was 4 m. As the SADCP was mounted on the drop keel, which was at ~6.5 m depth, there is no valid velocity data less than ~10 m depth. The observational uncertainties were 1-2 cm $s^{-1}$ [*Thurnherr*, 2010].

### 2.3 Underway Observations

A wide variety of meteorological and surface ocean data were collected by RV Investigator's underway data system, including wind speed and direction, rain, humidity, temperature, salinity, dissolved oxygen, fluorescence, turbidity, etc. (Supplemental Figure S1). These were output at 5 s intervals. During this period, the ocean surface data came in from ~6.5 m below the surface.

### 2.4 Operations

Three time series with a CTD cast every half hour were performed (Table 1). The first, Time Series 4 (TS4), lasted 51 hours and was on the east side of the Tiwi Islands (Figure 1). The second and third, Time Series 5 and 6 (TS5 and TS6), lasted 51 and 48 hours, respectively, and were on the west side of the Tiwi Islands (Figure 1 and Table 1).

| Site | Date (UTC 2019) | Start Time (UTC) | Duration (hours) | Latitude (° S) | | Longitude (° E) | | Water Depth (m) |
|---|---|---|---|---|---|---|---|---|
| TS4 | 14-16 Nov | 19:30 | 51 | 11 | 12.4 | 133 | 26.1 | 42 |
| TS5 | 22-24 Nov | 19:30 | 43+2 | 12 | 18.711 | 130 | 24.1 | 29 |
| TS6 | 3-5 Dec | 20:00 | 49 | 12 | 19.2 | 130 | 24.8 | 29 |

**Table 1. The date, time, latitude, longitude, and water depth for each of the Time Series during Leg 2 of IN2019v06.**

## 3 Modeling Support

To aid in understanding the circulation and tides in the region, simulations were performed for the region using the Regional Ocean Modeling System (ROMS) version 3.4. Simulations were used for two purposes. First, it was used to simulate the general circulation of the region to provide information on the areas surrounding the observation sites and second, to evaluate the performance of the vertical mixing parameterizations in ROMS, as was done in *Robertson and Hartlipp* (2017) and *Robertson and Dong* (2019). Whenever the first author obtains data that would be useful for in evaluating the vertical mixing parameterizations in ROMS, she adds to the previous evaluations in order to increase the range of conditions.

ROMS is a widely used, primitive-equation, sigma-coordinate model [*Shchepetkin and McWilliams*, 2004]. The general circulation model resolution was ~2 km with 25 levels. The mixing simulations had a resolution of 1 km, also with 25 levels. These simulations were run for 20 days. The mixing solutions were horizontally uniform over a very small domain, essentially making them 1-D. Bathymetry was obtained from Geoscience Australia [*Whiteway,* 2009]. The observed hydrography was used as much as possible for these simulations with additional values as needed from World Ocean Atlas [*Locarnini et al.*, 2014]. Tidal forcing used eight constituents, $M_2$, $S_2$, $N_2$, $K_2$, $K_1$, $O_1$, $P_1$, and $Q_1$, with the coefficients taken from TPXO8 [*Egbert and Erofeeva*, 2002]. These were applied to the 2-D mode elevations and velocities, updated on the 2-D steps. Winds were light during most of the observational period (Supplemental Figure

S1), so winds were not included in the general circulation simulation. Observational winds were used for the vertical mixing simulations, with the winds ramping up over the first day. The mixing solutions were also run for only 3.5 days and started a day before the time series in order to have the winds spin up over the first day. The daily solar forcing was included in all simulations using observed values. The *Large-McWilliams-Doney Kpp* (LMD) vertical mixing parameterization was used for the general circulation simulation and LMD, Nakanishi-Niino, and Mellor-Yamada 2.5 were used for the vertical mixing parameterization (Robertson and Dong, 2019). The model data was analyzed with *Pawlowicz'***s** T_tide package [2002] in addition to Matlab® scripts as required.

## 4 Results and Discussion

The SADCP velocities showed clear tidal ellipses (Supplemental Figure S2a-c) during all three time series. The simulated tidal ellipses from the general circulation simulation matched the observed ellipses (Supplemental Figure S2d-e), validating the simulation replicated the tidal velocities. Tidal residual currents were small, 1.5, 3.5, and 3.9 cm $s^{-1}$ for Time Series 4, 5, and 6, respectively when compared to the tidal velocity magnitudes, ~44, 48, and 26 cm $s^{-1}$, respectively. The clear tidal ellipses indicate that tides were the dominant forcing factor and other primary processes, such as major geostrophic currents, alongshore coastal currents, or eddies, did not play a significant role. This reduced the forcing factors to tides, along with winds, upwelling, and the daily solar radiation cycle. The winds were light except for primarily onshore sea breezes in the afternoon and evening. The weak winds, primarily on-shore, along with the weak Coriolis in the tropics were not conducive for strong upwelling. The daily thunderstorms did not reach the ship's location except for the first few hours of Time Series 5, so rain was not a major factor. Although inertial oscillations are a possible, the time series length (~2 days) is less than their period of ~2.3 days. Furthermore, the SADCP currents (Supplemental Figure S2) do not indicate their presence. Consequently, the relevant forcing factors were reduced to tides and the daily solar radiation cycle. This provides an excellent opportunity to examine tidal flow in isolation of strong background currents or eddies.

The hydrographic conditions differed between the east and west sides of the Tiwi Islands, although tides and solar radiation played major roles on both sides. Time series from the eastern side (TS4) were cooler, fresher, and higher in oxygen (Figure 2) than the time series (TS4) on the western side (TS5 and TS6) (Figures 3 and 4). A clear two layer structure with a thermocline and peak Brunt-Väisälä frequency > 10 cph at ~20 m was present on the eastern side (Figure 5c); whereas, temperatures and salinities on the western side were nearly uniform with depth (Figure 2). Temperatures fluctuations were largest at the surface and at ~20 m on the east side and at the surface on the west side (not shown). The surface fluctuations are attributed to the daily solar radiation and cooling cycles. The deepening of the warm temperatures from the daily solar radiation were mixed into the upper water column by the daily sea breezes (Figures 2-4). This is clearly seen in both the temperatures and densities (Figures 2a&c 3a&c, and 4a&c). It is also apparent as high Brunt-Väisala frequency values at the corresponding times and depths (Figures 5c, 6c, and 7c).

Model simulations for the locations of TS4 and of TS5 and TS6 from the general circulation simulations had similar hydrographic structure to the observations. The temperatures and salinities for TS4 were reproduced reasonably well (Supplemental Figure S3a from the circulation simulation); however, for TS5 and TS6, the structure was reproduced, but the water

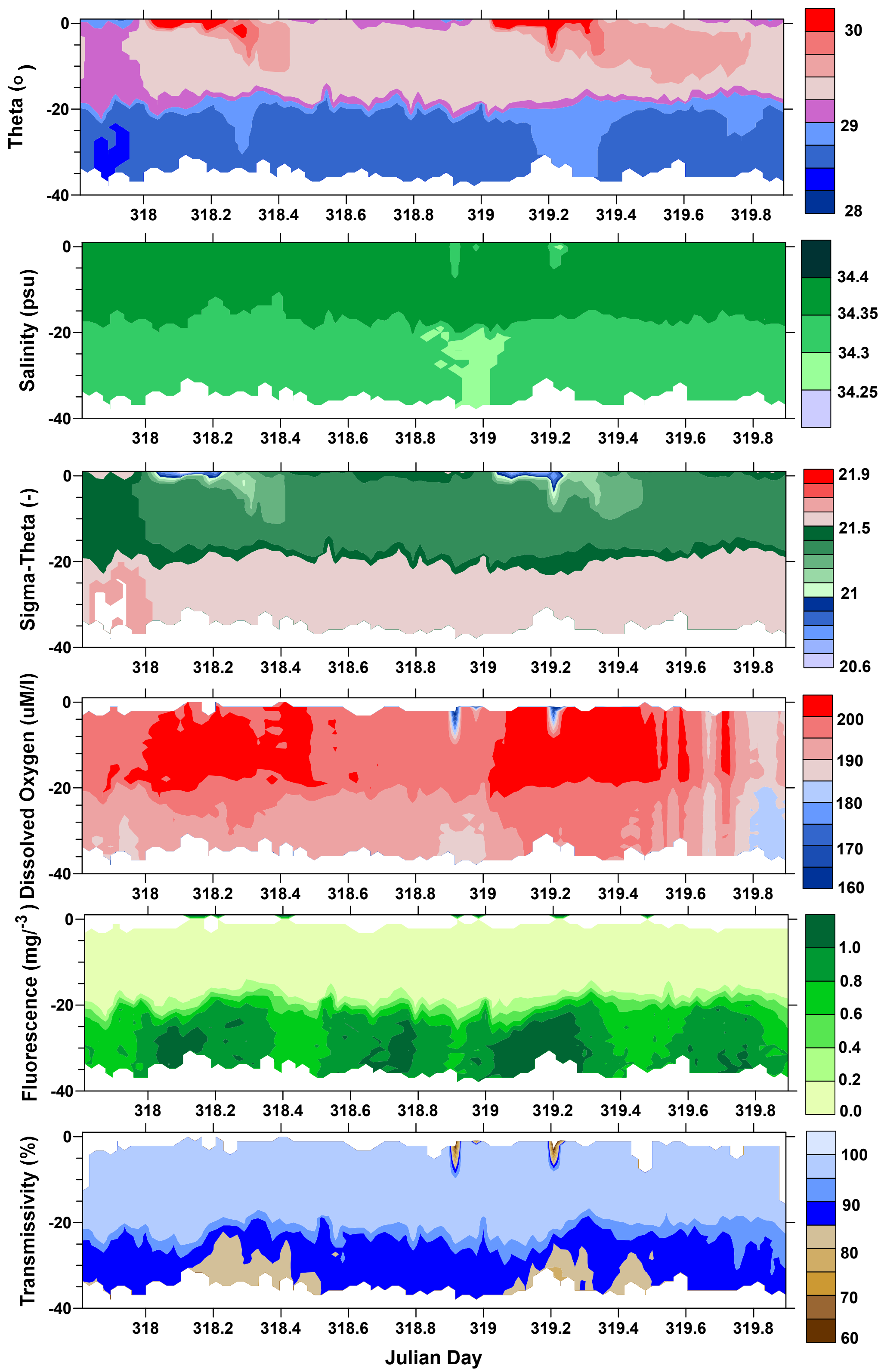


**Figure 2. a) Potential Temperature, b) Salinity, c) Potential Density, d) Dissolved Oxygen, e) Fluorescence, and f) Transmissivity during Time Series 4 on the east side of the Tiwi Islands.**

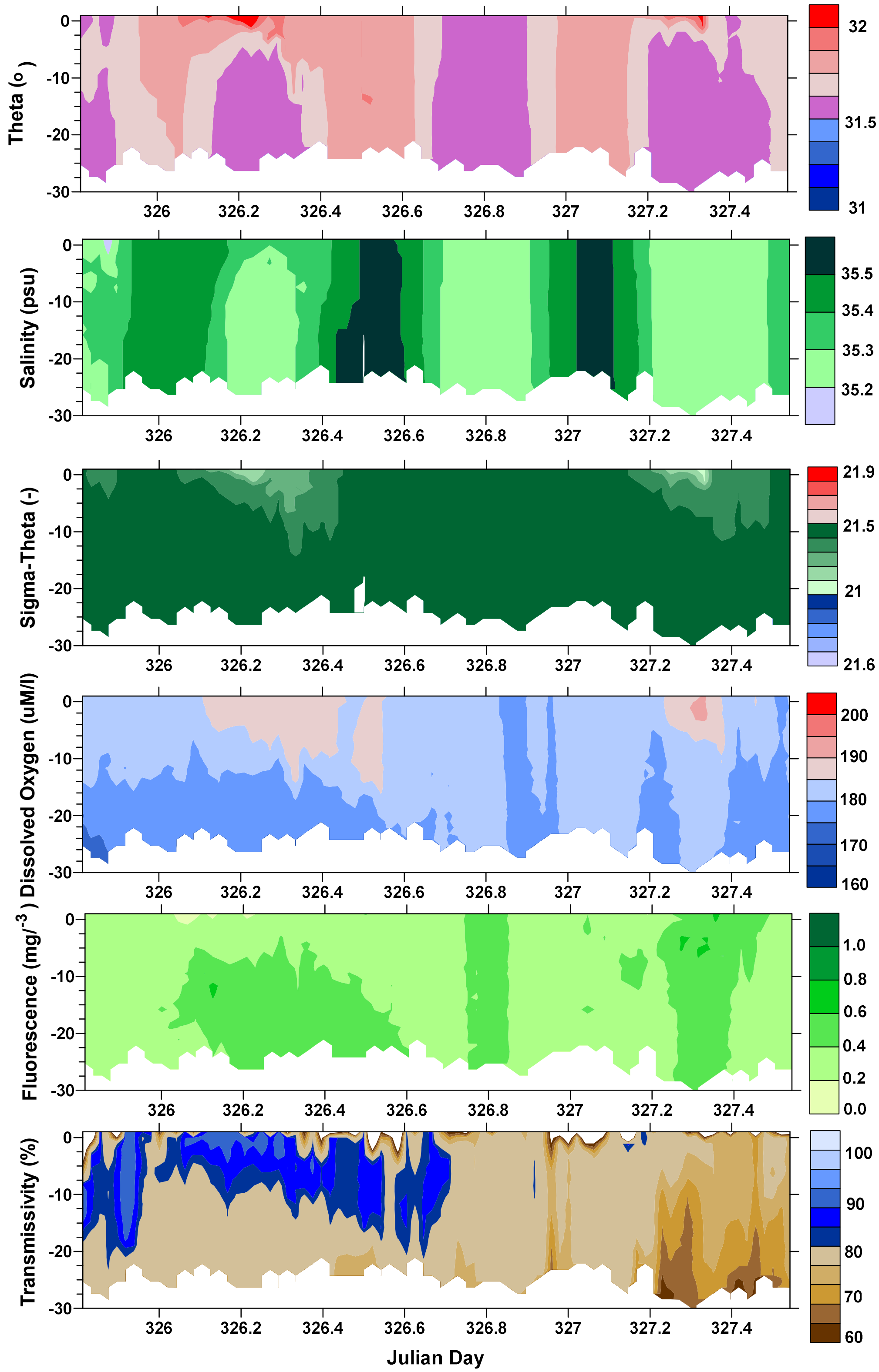


**Figure 3. a) Potential Temperature, b) Salinity, c) Potential Density, d) Dissolved Oxygen, e) Fluorescence, and f) Transmissivity during Time Series 5 on the west side of the Tiwi Islands.**

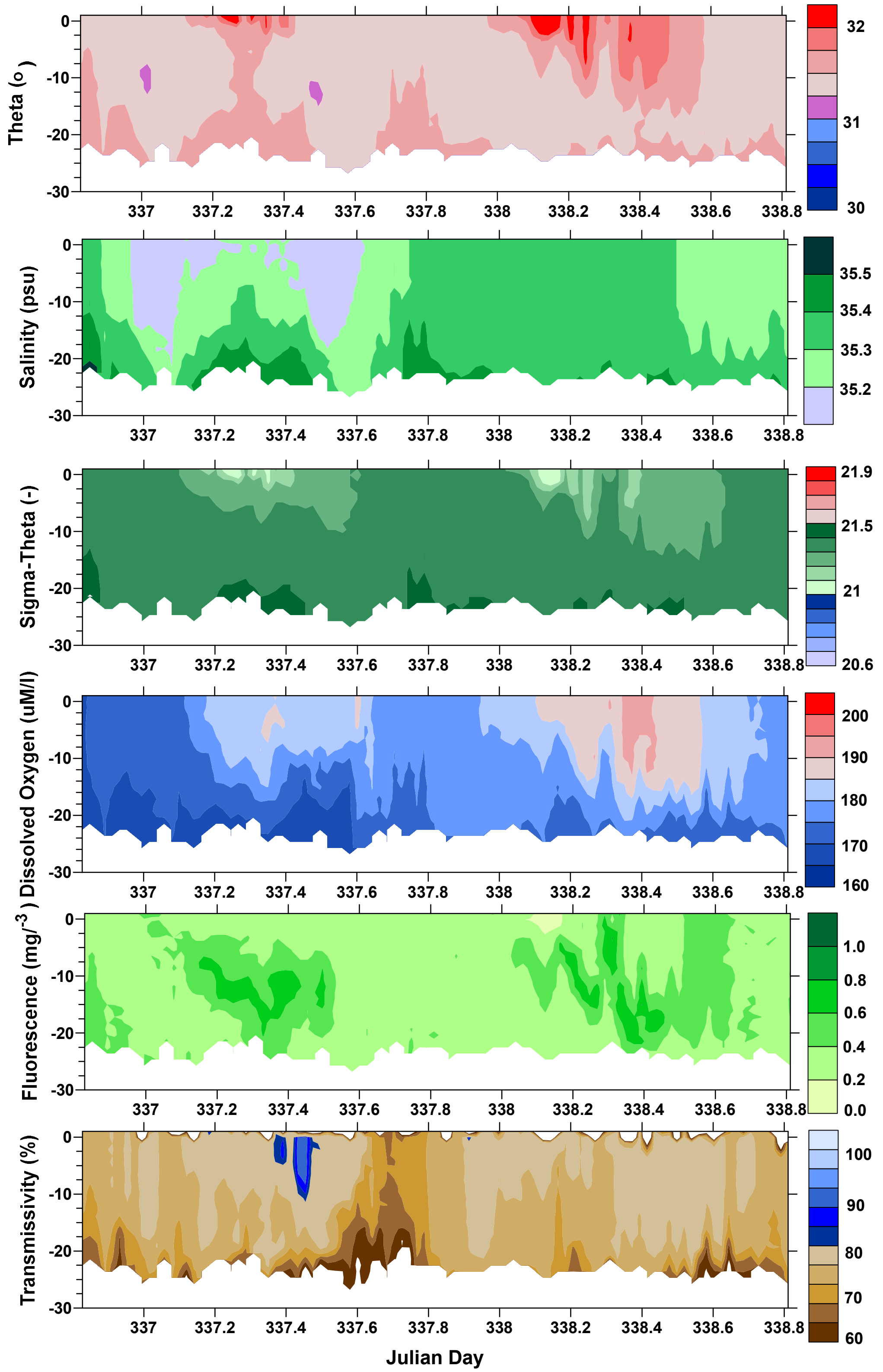


**Figure 4. a) Potential Temperature, b) Salinity, c) Potential Density, d) Dissolved Oxygen, e) Fluorescence, and f) Transmissivity during Time Series 6 on the west side of the Tiwi Islands.**

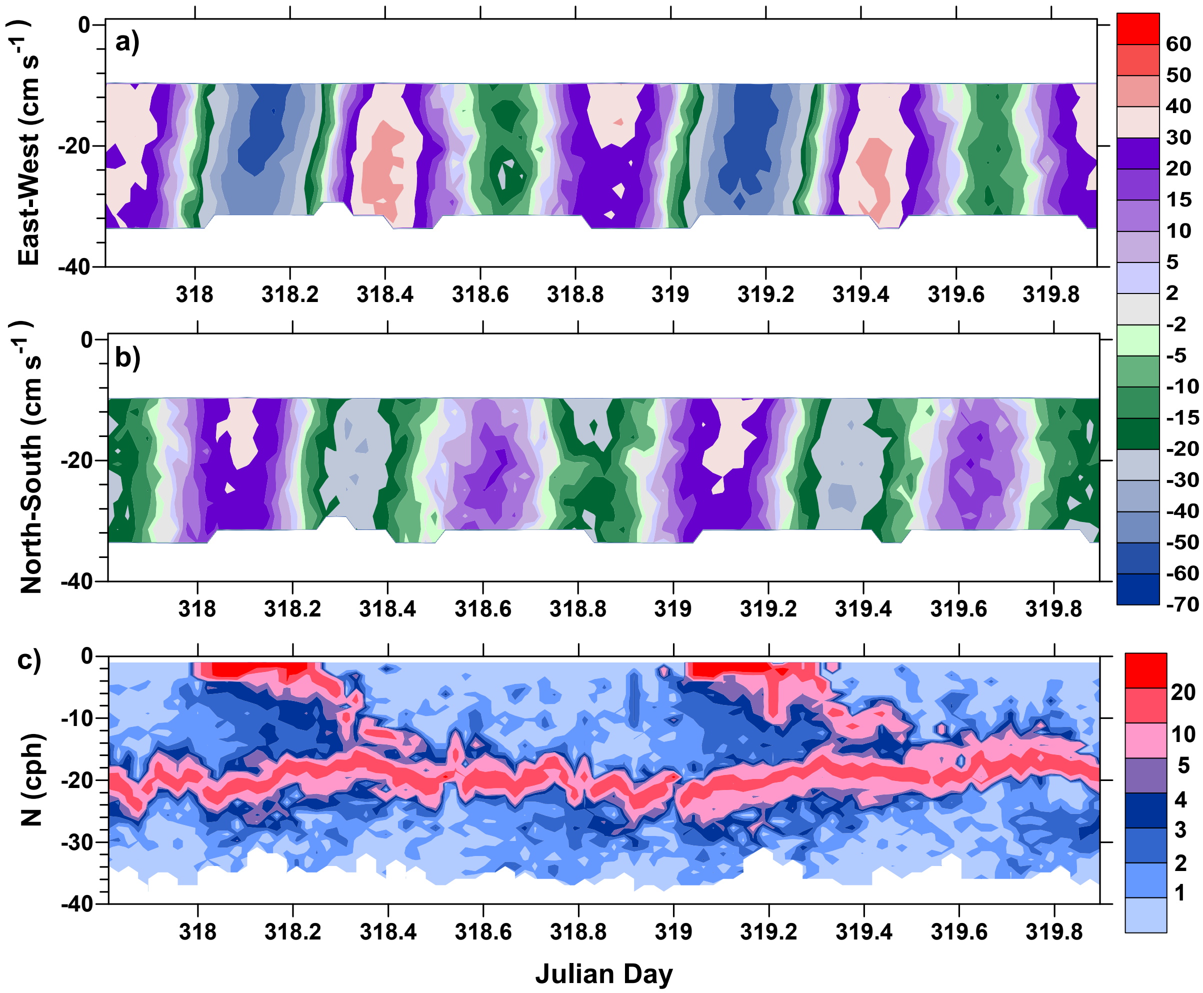


**Figure 5. a) The East-West and b) the North-South velocities during Time Series 4. c) The Brunt-Väisälä frequency during this time.**

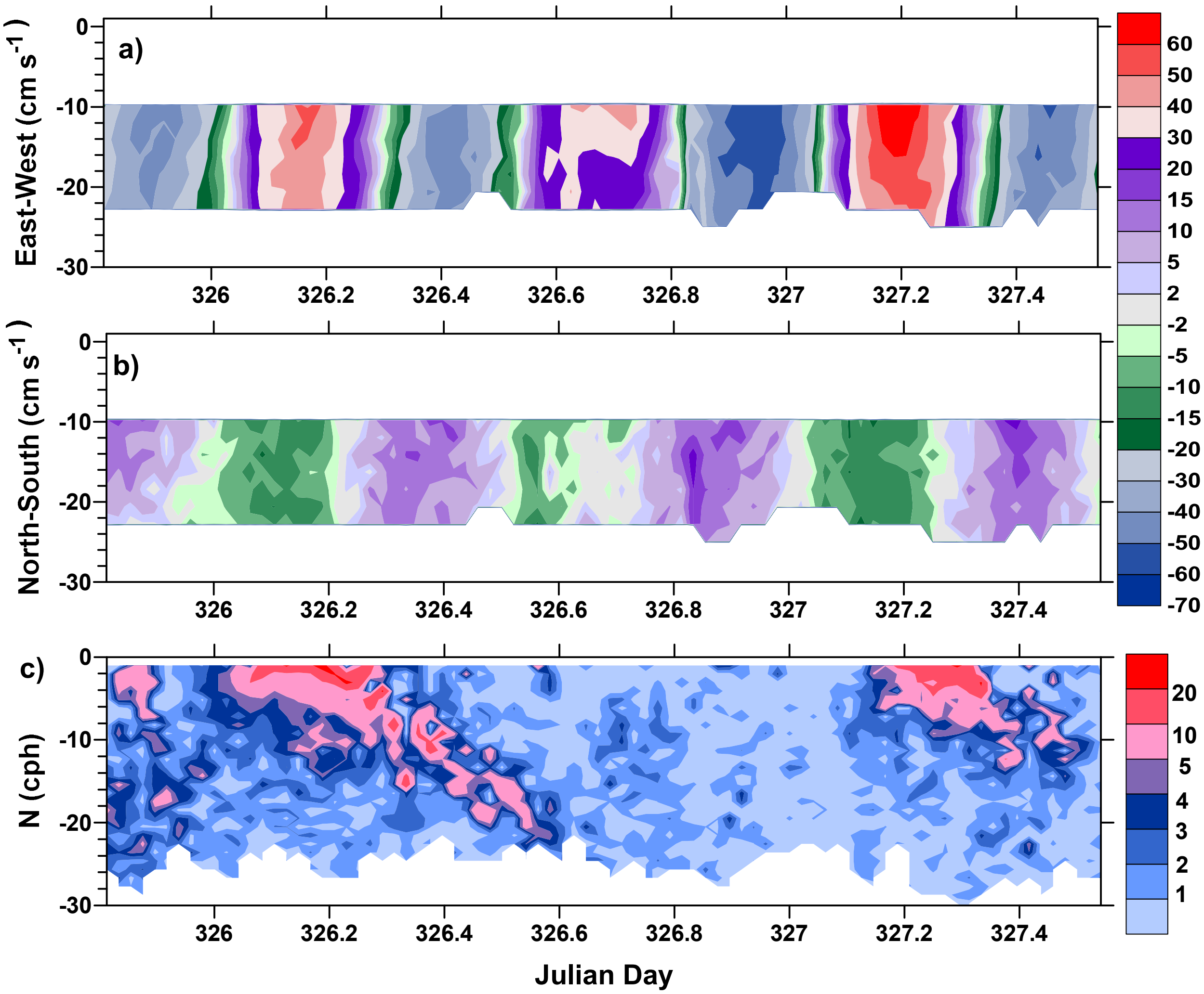


**Figure 6. a) The East-West and b) the North-South velocities during Time Series 5. c) The Brunt-Väisälä frequency during this time.**

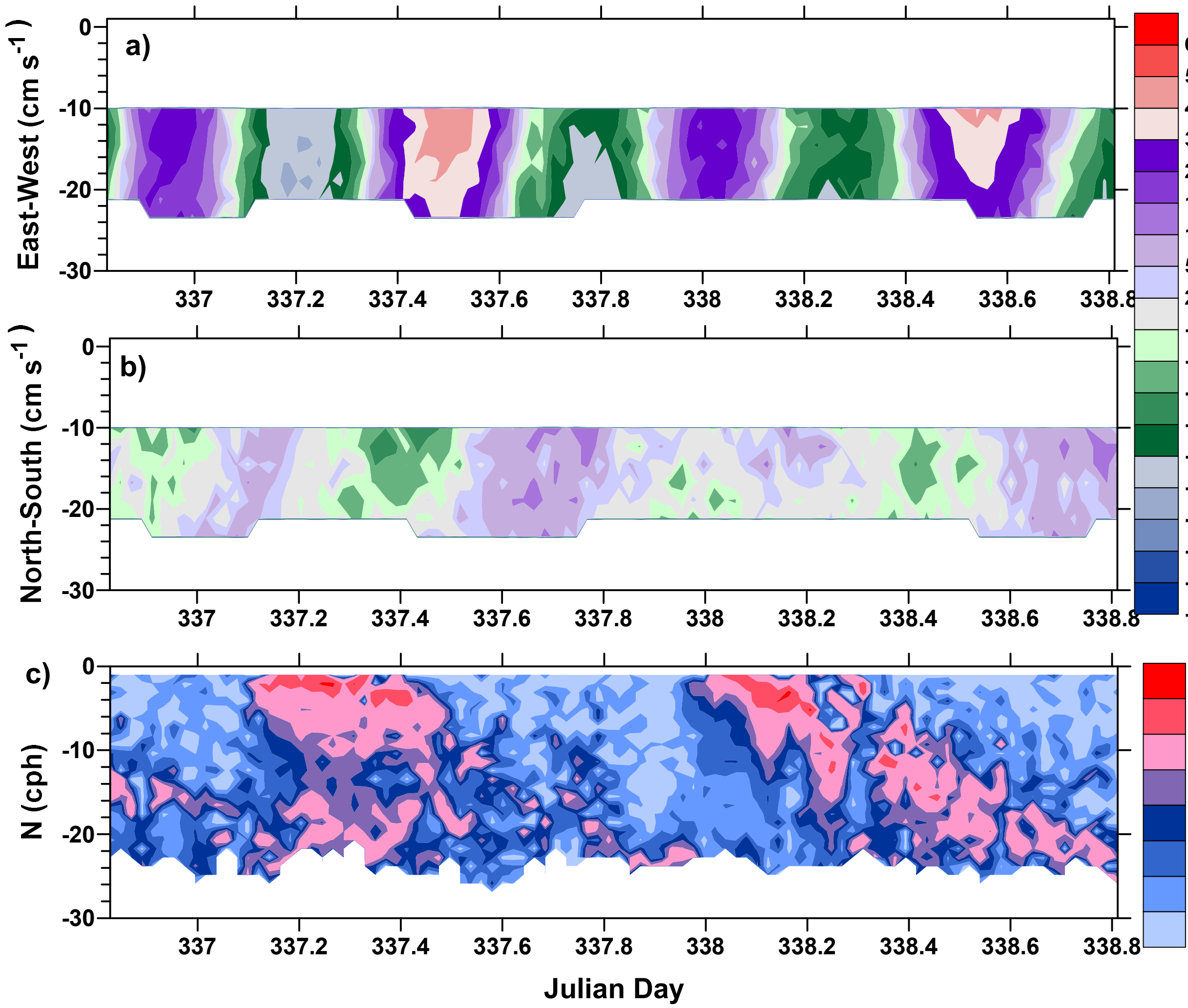


**Figure 7. a) The East-West and b) the North-South velocities during Time Series 6. c) The Brunt-Väisälä frequency during this time.**

column was too uniform vertically, too cool by ~0.75°C, and too fresh by ~0.35 psu (Supplemental Figures S4a and S5a for TS5 and TS6, respectively). South-North potential temperature and salinity transects of the model results on the west side showed a well-mixed water column both initially and at the end of the simulation (Supplemental Figures S6 and S7 for temperature and salinity, respectively). Similar transects on the east side replicated the two layer structure of TS4 with a tidal front developing only at the southern end adjacent to land and more apparent in salinity (Supplemental Figures S8 and S9 for temperature and salinity, respectively). The bottom of the lower layer did warm slightly, ~0.02-0.03°C, during the simulation, which is attributed to mixing and will be discussed later (Supplemental Figure S8).

Some additional insight into the hydrodynamics of the region can be gained from IMOS moorings. Temperatures from the nearby LYN mooring in 203 m water depth are well-mixed in the upper 50 m through most of the year and the velocities in the upper 50 m are essentially barotropic and tidal (Supplemental Figure S10), indicating that it is not unusual for the water column to be well-mixed in the upper 50 m in this area. The background currents alternate between east and west on roughly a 60 day cycle. LYN is north of the time series sites in deeper water nearer the continental shelf break and these alternating currents do not appear to affect the time series. Surface temperatures warm after day 300, reflecting the increased daylight hours. The IMOS mooring at Darwin, DAR, is in 12 m of water. Although the Darwin was not operational at the time of the voyage, it does indicate that typically the velocities are barotropic and strongly tidal (Supplemental Figure S11). Unfortunately, there are no IMOS moorings on the east side. However, the circulation simulation results indicate a two layer structure for the region, with a tidal front only at the southern end in water depths < ~30 m (Supplemental Figure S3).

Solar radiation played a significant role in the temperature, primarily at the surface. This warming can be seen in TS4 starting just before day 318.2 and 319.2 (Figure 2), in TS5 starting just before day 326.2 and 327.2 (Figure 3), and in TS6 starting just before day 338.1 (Figure 4). The impact of the warming depended on the cloud cover. It was often cloudy in the mornings and was cloudy most of day 337, decreasing the solar warming then. Day 338 was sunny and clear from early morning, with the increase in temperature commencing 0.1 of a day earlier and a >0.4 increase in temperature (Figure 5a), which was stronger than earlier in TS6 and in TS5. The influence of the solar radiation clearly reached to 10-15 m (Figures 2-4). The effect of the warmer water from the solar radiation is clear in the Brunt-Väisälä frequency, $N$, (Figures 5c, 6c, and 7c for TS4, TS5, and TS6, respectively). $N$ is high at the surface during warming and sinks in the water column until it reaches the thermocline (~20 m) for TS4 (Figure 5c) or the bottom for TS5 and TS6 (Figures 6c and 7c, respectively). Nighttime longwave radiation cools the surface, lowering the surface $N$ from > 15 cph to a background value < 3 cph (Figures 5c, 6c, and 7c,).

During TS5, there was one brief rain storm over the ship dropping 7-8 mm of rain, which started a quarter of an hour after the first TS5 cast and ended before the third cast. The rain storm can be seen as an anomalously low salinity (Figure 3b) and potential density (Figure 3c) in the upper 6 m before day 326; however, the lowest salinity occurred 1 hour after the rain storm. Since there were other rain storms scattered in the vicinity and runoff from rain storms on land, this minimum is believed to be from rain in another location being advected past the ship.

Winds followed a daily sea breeze pattern reaching 8-10 m/s, with the exception of TS5 (Supplemental Figure S1). Winds were stronger 14 m/s from the NW during the first day of TS5, then reduced to ~2 m/s during the second day (Supplemental Figure S1c-d).

In addition, to the influence of the solar radiation and nighttime cooling, tides played a huge role in the dynamics for this region. The tides in nearby Darwin are quite large with a tidal range exceeding 7 m (http://www.bom.gov.au/oceanography/projects/ntc/nt_tide_tables.shtml). TS4 was collected during a spring tide, TS5 and TS6 near neap tides. Nevertheless, the tidal ranges for TS5 and TS6 of ~4 m and ~2 m respectively, were nearly the same range as that for TS4 of ~3 m. These tidal ranges were estimated from the maximum pressure converted into depth combined with the altimeter reading. Tidal currents were much stronger on the western side than the eastern side with velocity magnitudes of 48 cm/s and 26 cm/s during neap tides against 44 cm/s during spring tide (Figures 5-7). Stronger tides in the west agreed with stronger tides on that side in the TPX08.2 estimates (not shown). Semidiurnal tides dominated on both sides of the Tiwi Islands (Figure 8). The net mean currents on the west side were much stronger, 3.5-3.9 cm/s than for the east side with 1.5 cm/s. The baroclinic anomaly velocities, defined as the difference between the velocity and the depth-averaged velocity, were roughly equivalent on both sides, ranging from 5-10 cm/s (Figure 9). The East-West velocity dominated at all sites, with the tidal ellipses ~6$^{o}$ off the horizontal. At TS 4, the North-South velocity played a larger role with a magnitude of ~67% of the East-West velocity; however, it was well correlated (0.9) with the East-West velocity, lagging by ~1.5 hours (Supplemental Figure S12a).

Despite the major forcing processes on both sides of the Tiwi Islands being tides and solar radiation, the dynamics differed between them. On the western side, strong tidal advection dominated; while on the eastern side, a two-layer internal tide was present. Since the tidal currents dominated, tidal advection can be identified through correlations. Looking at correlations for TS4, changes in potential temperature (Supplemental Figure S12) and salinity (Figure 10a) below 20 m lagged changes in the East-West velocity by ~3 hours with a correlation of ~ 0.8 (positive changes with a southward flow). Changes in the upper water column had the opposite correlation sign (Figure 10a). For TS5, correlations of the East-West velocity with the salinity (Figure 10b) (~0.8) and potential temperature (Supplemental Figure S13a) indicate that the salinity changes ~2-3 hours after the East-West velocity changes (positive change with a westward flow). The correlations were weaker for TS6 (Figure 10c) and limited to below 20 m

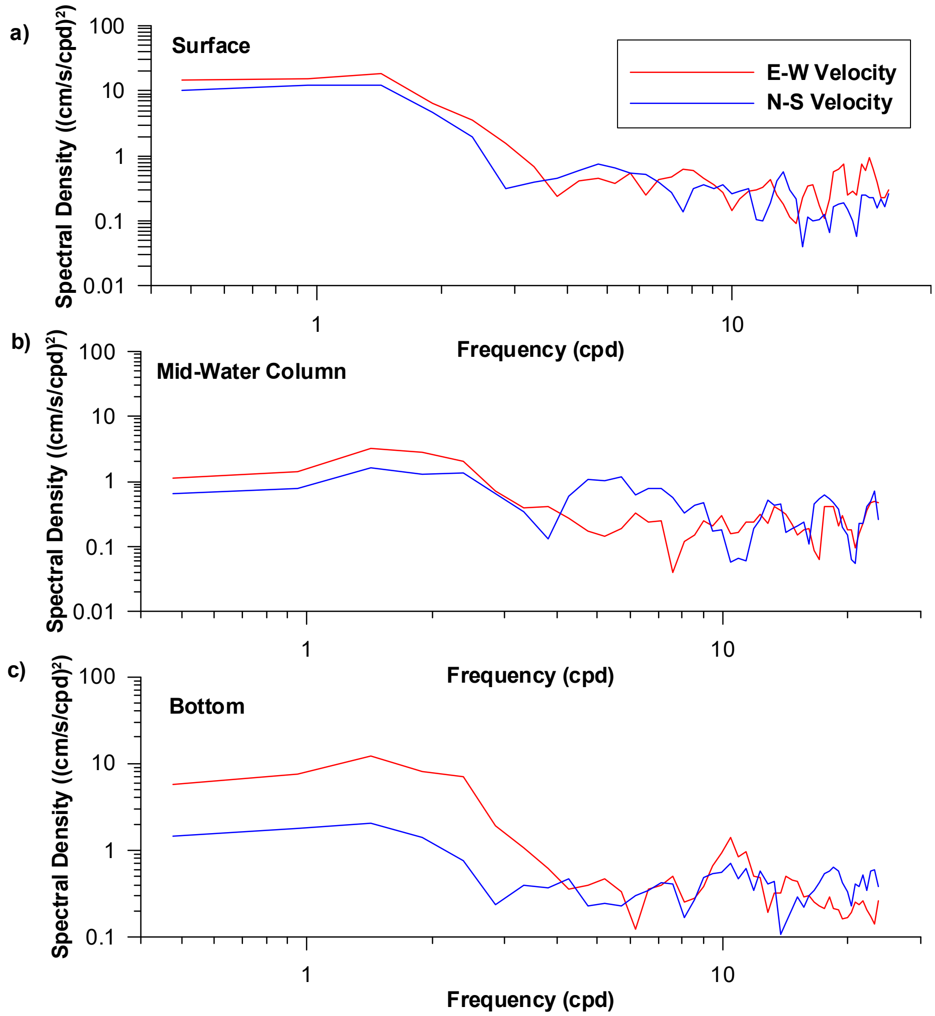


**Figure 8. Spectra of the baroclinic anomalies for the East-West (red) and North-South (blue) velocities during Time Series 4 at the a) uppermost, b) middle and c) lowest shipboard ADCP level.**

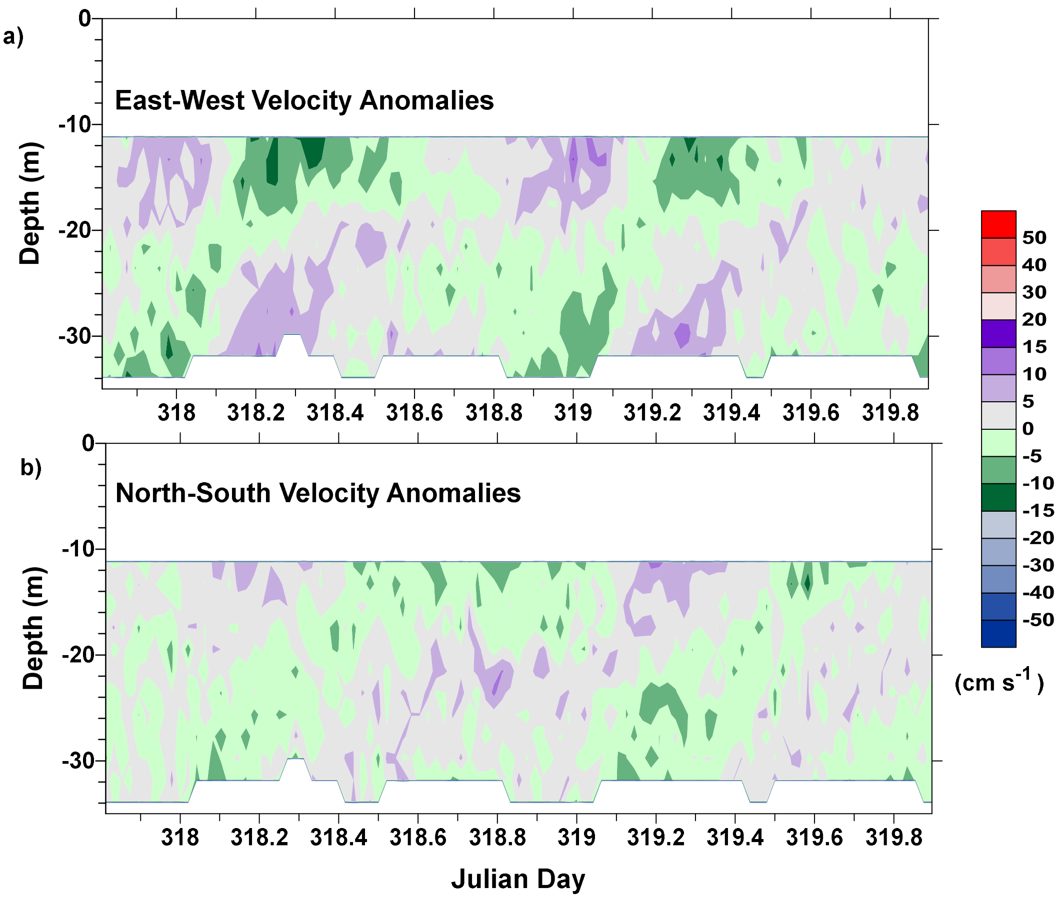


**Figure 9. The baroclinic anomalies in the a) East-West and b) North-South velocities during Time Series 4.**

depth (~-0.7) with a lag of ~2 hours (positive change with a westward flow). On the eastern side, potential temperature changed in the deeper layer by < 0.2ºC during half of a semidiurnal tidal cycle during TS4 (Figure 11a), while the salinity changed < 0.05 psu (Figure 11d). In Figure 11, the red profiles were taken from a time with maximum eastward flow, the blue line from a time with a maximum westward flow, and the black line from a time with minimum velocities. The profiles from TS5 and TS6 were selected in a similar manner; however, the times were adjusted by 2 hours for TS5 and TS6, based on the correlations. Changes in potential temperature and salinity in the lower water column were much larger for TS5 with potential temperature changes of ~0.5ºC (Figure 11b) and > 0.15 psu (Figure 11e). Salinity changes for TS6 were roughly the same as for TS5 (Figure 11f); however, the temperature changes were less than half as large (Figure 11c). Focusing on the lower water column to avoid density changes due to the daily solar warming, density changes were greatest during TS6 (Figure 11i) and equivalent between TS4 and TS5 (Figures 11g and 11h, respectively). It is clear in Figure 11, that temperature plays a bigger role in density changes in the east (Figure 11g) and salinity plays a bigger role in the west, particularly for TS6 (Figures 11h and 11i). This indicates that warmer water was advected from the southeast at TS4 and warmer, saltier water from the east at TS5 and TS6. Depths were shallower to the southeast and south of TS4 and to the east of TS5 and TS6.

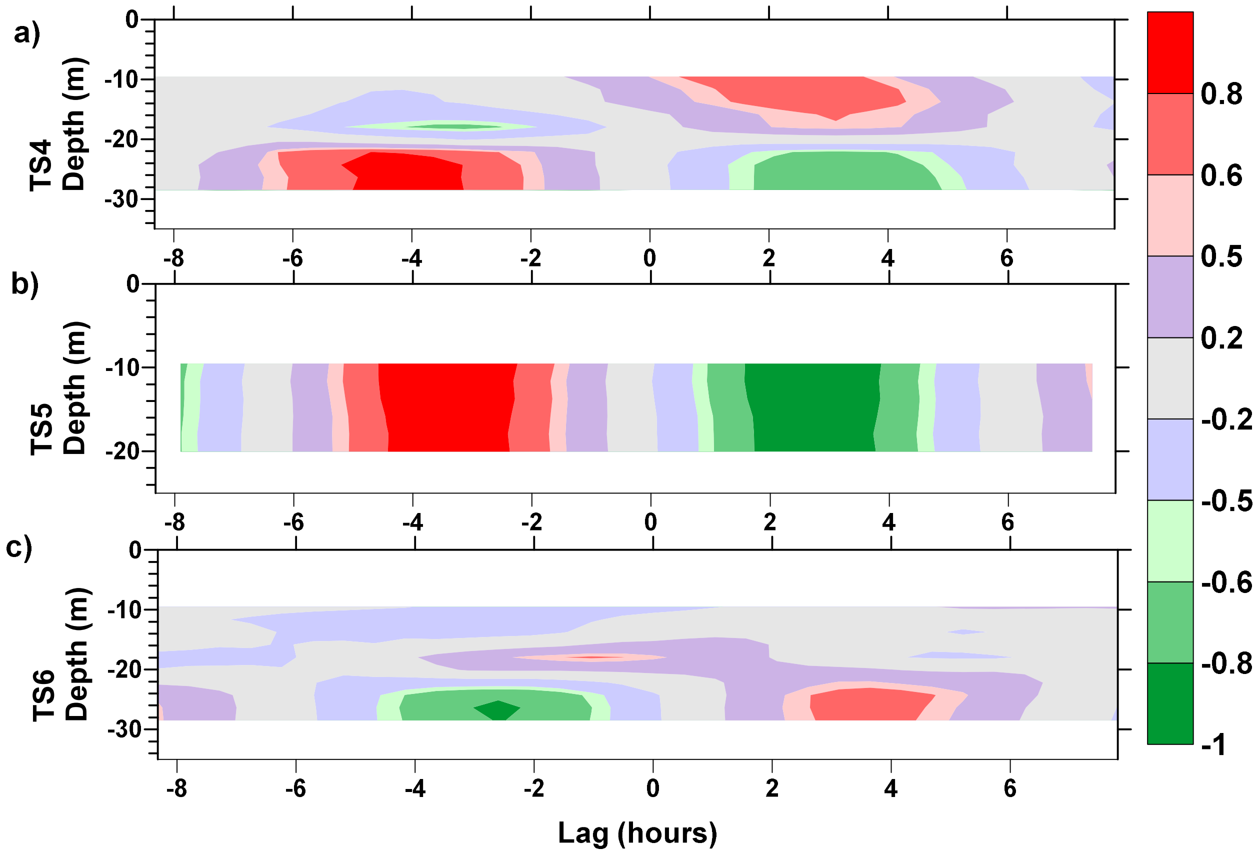


**Figure 10. Lagged correlations with depth between the East-West velocity and salinity for a) Time Series 4, b) Time Series 5, and c) Time Series 6. The East-West velocity was the strongest in all cases. Salinity was used to reduce influences of the daily solar cycle in temperature.**

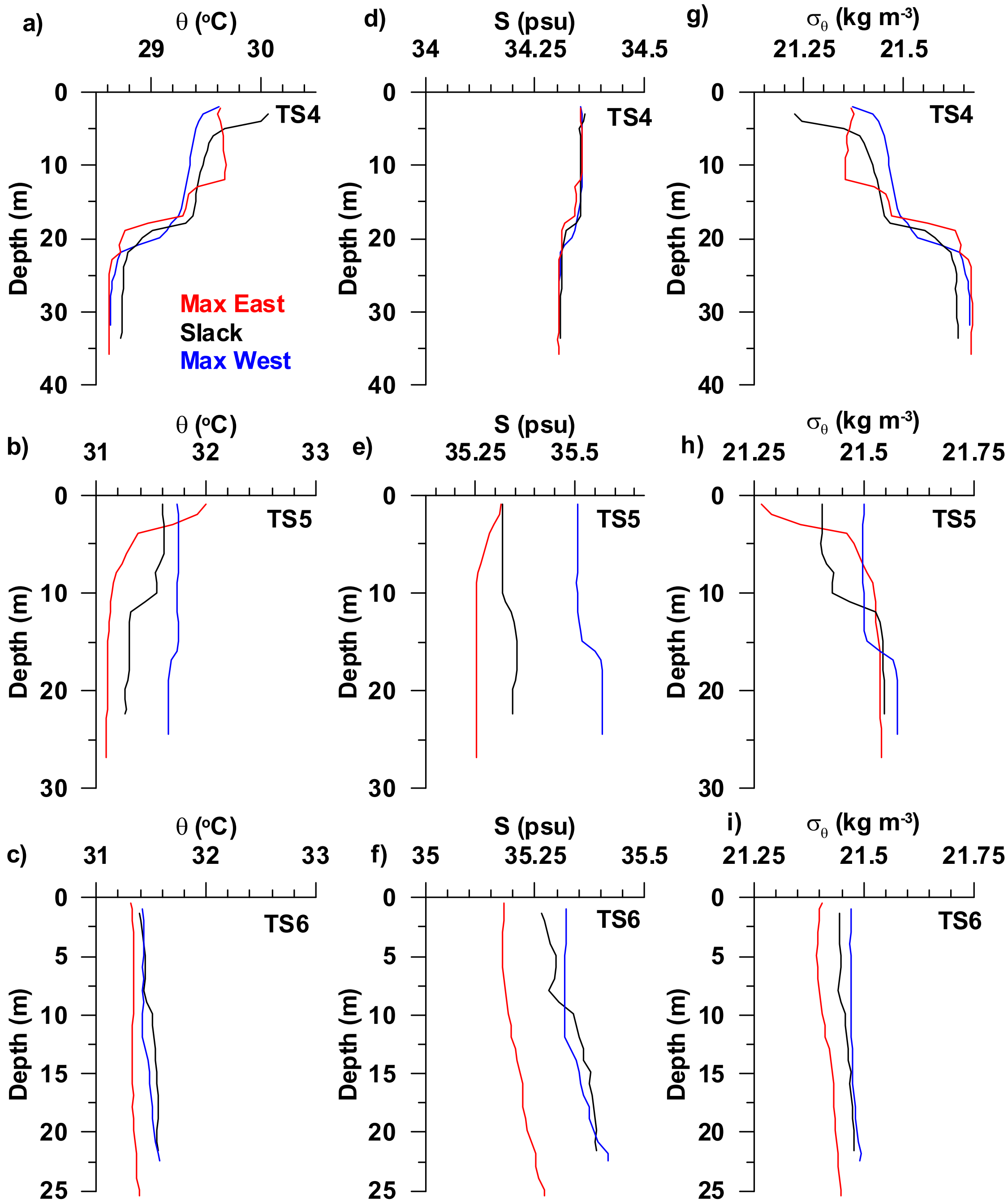


**Figure 11. Profiles of a-c) potential temperature, d-f) salinity, and g-i) potential density during Time Series 4 (a, d, g), 5 (b, e, h) and 6 (c, f, i) from the times of the maximum eastward (red) and westward (blue) velocities and slack tide (black).**

During TS4, the water column had two distinct layers, separated at about 20 m (Figure 2). The baroclinic anomalies indicated an upward propagating phase (downward propagating energy) at a diurnal frequency and a very slow speed (~$8x10^{-4}$ m $s^{-1}$) (Figure 9). Empirical Orthogonal Function (EOF) analysis on the baroclinic anomalies indicated a strong diurnal signal in both the East-West and North-South velocity anomalies of 64% and 44% (Figure 12a and 12c, respectively). These diurnal signals not only contain the diurnal tides, but also the daily solar radiation and sea breeze cycles and the daily signal in the winds (Supplemental Figure S1). Both of the first two EOFs were low modes, with the first EOF a two-layer internal tidal cycle, and the second intensified velocities at the thermocline and opposite velocities in the upper and lower layers compared to the thermocline (Figure 12b and 12d for the East-West and North-South velocities, respectively). Higher mode signals were also present (Supplemental Figures S14-S19).

Dissolved oxygen concentrations, fluorescence, and transmissivity also differed between the eastern and western time series. Dissolved oxygen concentrations were much higher on the eastern side (Figure 2d) than on the western side (Figures 3d and 4d); however, both increased as the warmer water from solar radiation reached deeper in the water column. Fluorescence on the western side (Figures 3e and 4e) was high throughout the water column, whereas on the eastern side, high fluorescence was restricted to below the thermocline (Figure 2e). When integrated over the water column, the fluorescence on the eastern side was roughly twice that on the western side (not shown). Transmissivity was high when and where the fluorescence was high (Figures 2e, 3e, and 4e), with the exception of the first day of TS5, where there was low transmissivity in the upper water column roughly corresponding to the warmer temperatures from solar radiation and high dissolved oxygen (Figure 3f). This is the time of the strongest winds, ~14 m/s from the Northwest.

The underway data show warmer temperatures on the western side than the eastern side, particularly in the shallow water south of the Tiwi Islands (Supplemental Figure S20). Likewise, salinity is generally higher on the western side than the eastern side (Supplemental Figure S21).

The primary dynamics on the western side appear to be tidal advection along with the daily solar radiation/night time cooling and sea breeze cycles. Waters to the east of the TS5 and TS6 sites were warm, salty and denser (red lines in Figure 13) than water west of these sites (blue lines in Figure 13). The water is very shallow east of the time series sites and TS5 and TS6 were collected in spots that were slightly deeper than their surroundings. Warming of the water column and evaporation affect shallower water more than deeper water, increasing the temperature and salinity more than in deeper water. In the deeper water to the west of the Time Series sites 5 and 6, the water is cooler and fresher. Most of the variation in the temperature and salinity that occurred during the time series are believed to be alternating advection of the warm, salty water from the shallower water depths to the east during a westward flow and cooler water from the deeper locations to the west during an eastward flow. The increases in salinity outweigh the increase in temperature, generating denser water that sinks as it travels offshore (Figure 4). Cooler, fresher water (black lines in Figure 13), such as that in the trench (Figure 1), replenish the inflow waters. Mixing homogenizes the water column. The warmer waters from the shallow regions also are high in dissolved oxygen, turbidity, and fluorescence. The western side had extensive shallow regions, not only south of the Tiwi Islands (Figure 1), but also to the west (not shown). The influence of the shallow water on the western side was supported by the

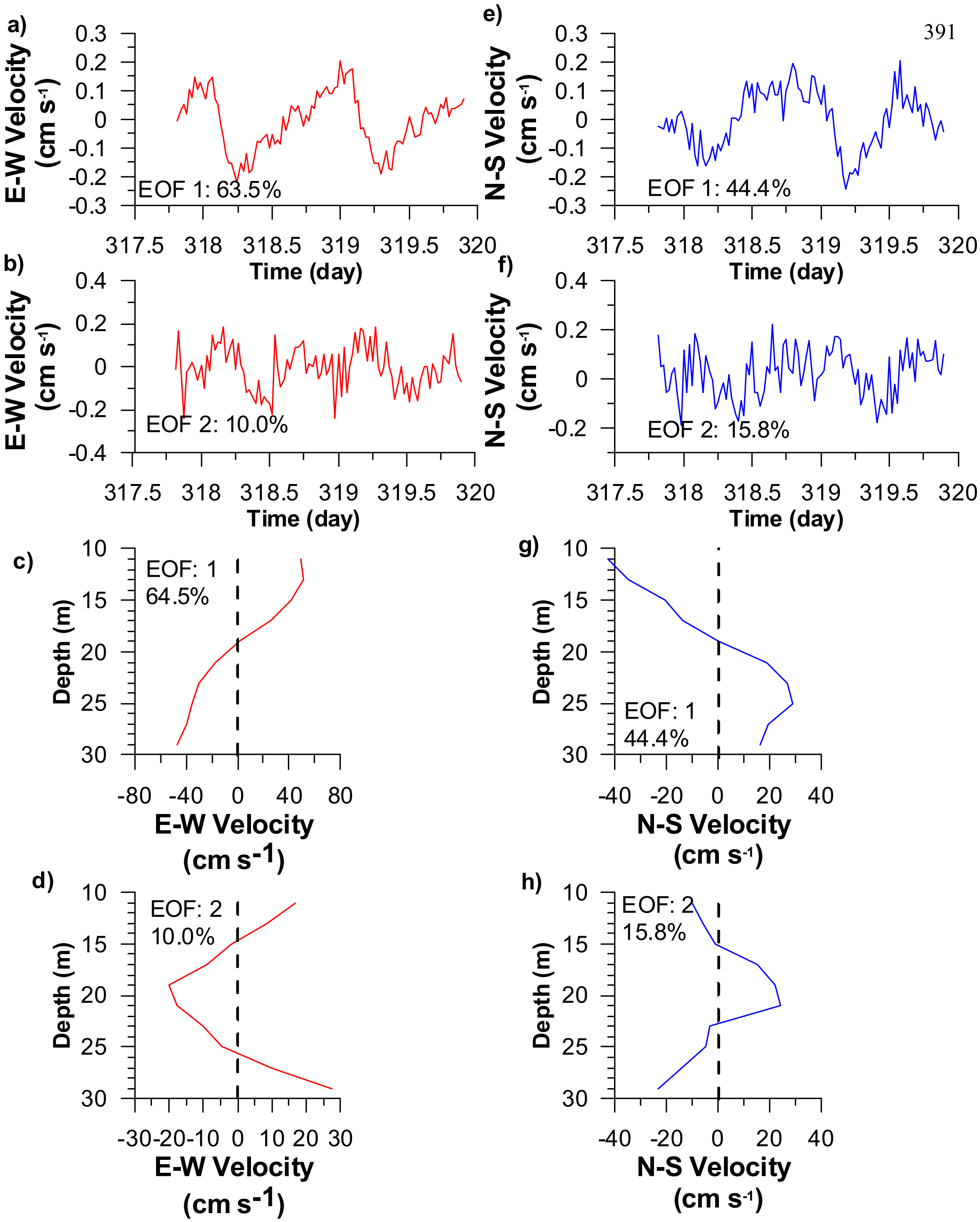


**Figure 12. The first two EOFs for the a-d) East-West and e-h) North-South velocities, during Time Series 4, showing the a, b, e, f) time dependence and c, d, g, h) depth dependence. The eigenvalues are given.**

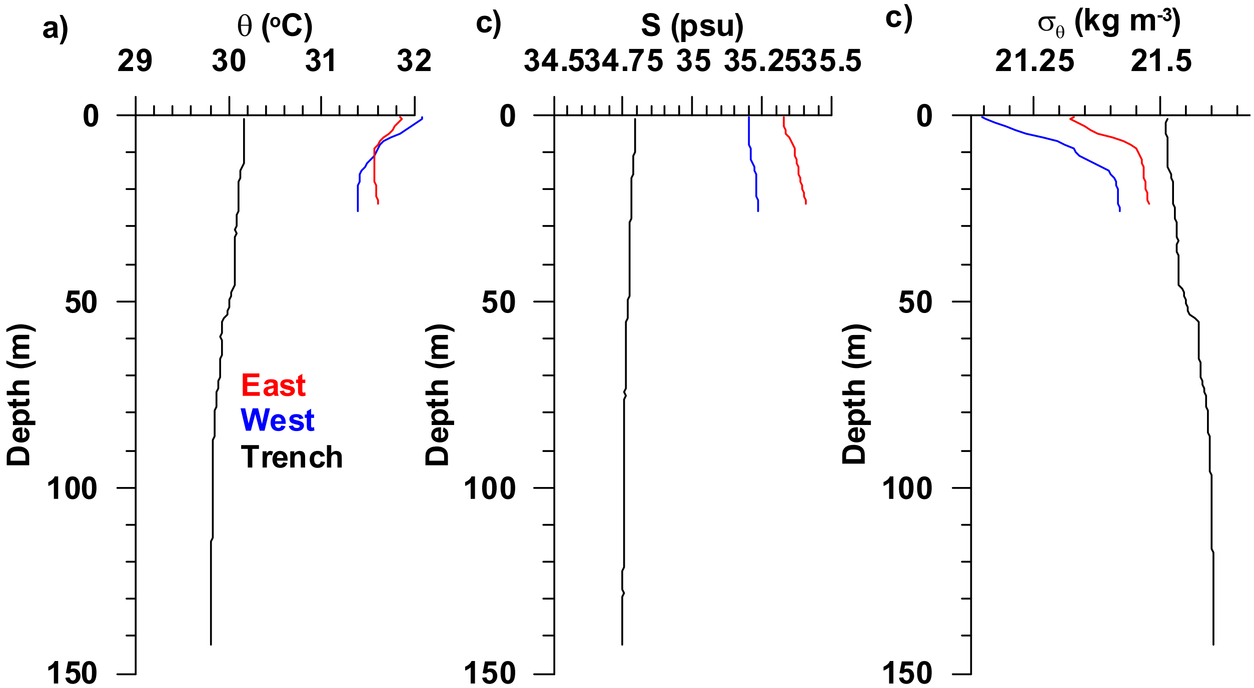


**Figure 13. Profiles of the a) potential temperature, b) salinity, and c) potential density with depth from a site in shallow water east of Time Series 5 and 6 (red), a site in deeper water west of Time Series 5 and 6 (blue), and in a trench west of Tiwi Islands (black).**

modeling study, which showed warm, saltier water forming in the shallow waters around these time series sites and moving offshore at depth. The model also indicated a westward flow of the waters formed in the shallow waters east of the Tiwi Islands. The shallower waters surrounding TS5 and TS6 also block the flow of cooler water reaching these sites.

A trench was a potential water source for the western side (Figure 1). A short time series, TS8, with ten CTD casts covering a 9 hour period was collected at the southern end of a trench. TS8 had cooler, fresher water (Supplemental Figure S22) than TS5 and TS6 (Figures 3 and 4). TS8 was also higher in dissolved oxygen and fluorescence than TS5 and TS6 (Supplemental Figure S22). TS8 occurred slightly after a neap tide and shifted from a southerly to northerly flow (Supplemental Figure S23b), but unfortunately we did not collect a complete diurnal or semidiurnal cycle. The water column was stable in the upper 10 m with the strongest stratification between 20 and 30 m (Supplemental Figure S23c). The East-West velocities were slightly baroclinic in the upper 70-80 m with peak velocities ~40 m (Supplemental Figure S23a).

On the eastern side, the dynamics were dominated by a two-layer internal tidal system with the transition at 20 m along with the daily solar radiation/night time cooling. The upper layer was warmer and saltier than the lower layer. It also had lower turbidity and fluorescence. The lower layer was cooler, fresher, more turbid, and higher in fluorescence. The daily solar cycle increased the stratification in the upper layer and this increase sank in the water column with time to the thermocline, with the surface temperature cooling overnight. In general, the water column was deeper on the eastern side than the western side.

The fluorescence behaved differently during the different time series; however, it responded to the daily solar cycle for all the time series, increasing just after the surface started warming. *Cloern* (1991) and *Sharples* (2008) have found the fluorescence to be correlated with the tidal cycles. On the eastern side, Time Series 4, there was a strong 12.4 hr signal and a weaker 6 hr signal in the fluorescence, which coincides with the semidiurnal tide and the entrainment and sinking of particles due to changes in the tidal velocities, respectively (Figure 2). Since fluorescence was higher only in the lower layer, correlations are only high in the lower layer (Supplemental Figure S12f-g). The daily lag between the velocities and the fluorescence was depth dependent. On the western side, there was a weak, deeper fluorescence signal for Time Series 5 (Figure 3) and a stronger signal for Time Series 6, which followed the daily solar cycle with higher fluorescence below the warmer temperatures and higher dissolved oxygen levels of the daily cycle (Figure 4). There was no evidence of 6 or 12 hr cycles in the fluorescence on the western side. The lags for the fluorescence were weak for TS5 and strongest for the East-West velocity at -4 hours. The lags were also depth dependent on this side (Supplemental Figures S13f-g and S24f-g for TS5 and TS6). So despite strong tidal advection on the western side, tidal effects on the fluorescence were weak.

Unfortunately, there were no dissipation observations during the profile time series. The water depth was too shallow to accurately estimate dissipation or diffusivities from the temperature and salinity measurements; however, Thorpe displacements were determined using the standard method of resorting the density profiles and determining the shift. The Thorpe displacements for the three time series indicate overturns reaching to the thermocline on the east side (Supplemental Figure S25a) and to 25 and 20 m on the west side for TS5 and TS6, respectively (Supplemental Figure S25b and c), during nighttime cooling events.

Simulations can add insight into mixing and the performance of the different mixing parameterizations. Two types of simulations were performed: a 3-D general circulation simulation using the LMD vertical mixing parameterization including only tidal forcing and solar radiation and a set of horizontally uniform simulations with tidal, solar, and wind forcing and the NN, MY, and LMD vertical mixing parameterizations. The latter set of simulations were executed to evaluate the performance of the vertical mixing parameterizations similar to *Robertson and Hartlipp* (2017). These simulations used winds as observed during the measurements. The winds do not start until the end of the first day, so the first day should be ignored and comparisons made starting at day 1. The first day is shown to indicate the initial conditions.

Differences between the simulations, both the simulations and the observations, and the different vertical mixing parameterizations will be discussed. This vertical mixing parameterization evaluation is based solely on temperatures and salinities from the observations and mixing models. Only the temperatures are shown, since the salinity observations are noisier and added little information. The general circulation and mixing simulations performed similarly for TS4 (Supplemental Figures S3 and S26, respectively), but quite differently for TS5 and TS6 (Supplemental Figures S4-5 and S27-28, for the general circulation and mixing simulations, respectively). The general circulation simulation had a semidiurnal signal for TS5

(Supplemental Figure S4), whereas the mixing simulation showed a cooling trend (Supplemental Figure S27). However, for TS6, the general circulation simulation has a cooling trend (Supplemental Figure S5) and the mixing simulation shows a daily cycle (Supplemental Figure S28). Since the mixing simulations are horizontally uniform, different water types did not advect past the site. Consequently, the semidiurnal tidal advection signal is absent. The temporal response for TS6 is a result of the daily solar cycle, not advection. Thus, these horizontally uniform simulations cannot replicate the observations in areas where tidal advection dominates. When compared to the observations, it is clearly apparent that none of the simulations did replicated the high frequency fluctuations of the observations (Supplemental Figures S26d-S28d), despite the observations having a 30 min sampling rate and the mixing model simulations a 5 min sampling rate (Supplemental Figures S26a-c-S28a-c). Nor did the general circulation simulations reproduce the high fluctuations, although the semidiurnal cycle was present (Supplemental Figures S3-S5). Also the daily solar radiation cycle was not reproduced in the simulations, except to a slight extent for TS6 by NN and MY (Supplemental Figure S28). The general circulation simulation was too cool for both TS5 and TS6, as mentioned earlier. However, the barotropic fluctuations of TS6 were reproduced by the general circulation simulation. Due to the influence of the daily solar cycle, NN and MY temperatures were roughly similar for TS6, but their range was less than that of the observations, reflecting the missing tidal advection. The LMD simulation for TS6 was too uniform and too warm and did not replicate the observations well.

Looking at the model estimates for the temperature diffusivity, only the simulations can be compared, since there were no diffusivity observations. A few researchers have used full depth velocity profiles to estimate diffusivities in a tidal flow (*Lozovatsky et al.,* 2008); however, our profiles did not include the benthic boundary layer, making this technique impractical due to high uncertainties. For TS4, the general circulation simulation indicated strong benthic mixing (Supplemental Figure S3c) as did the LMD (Supplemental Figure S29c) and MY mixing simulations (Supplemental Figure S3b). The LMD estimates were very large even for the background values, $> 10^{-4}$ $m^2$ $s^{-1}$(Supplemental Figure S29c). NN and MY background values were much smaller, $\sim 10^{-6}$ $m^2$ $s^{-1}$ , equivalent to the accepted background diffusivity for the deep ocean (Supplemental Figure S29a-b); however, they still had very high surface values, $>10^{-2}$ $m^2$ $s^{-1}$, and MY's benthic values were quite large, $>10^{-2}$ $m^2$ $s^{-1}$. All three vertical mixing parameterizations showed increased mixing on a daily time scale at the surface and with MY at a semidiurnal interval at depth (Supplemental Figure F29b). For TS5, all three vertical mixing parameterizations indicated extremely high diffusivities, $>10^{-2}$ $m^2$ $s^{-1}$ throughout the water column at various time intervals (Supplemental Figure S4). NN had the lowest diffusivity estimates. These high diffusivities were likely the cause of the barotropic nature of the temperatures (Supplemental Figure S27); however, the cooling of the water column was likely due to excessive night time cooling. The general circulation simulation also had lower vertical diffusivities, generally $<10^{-}$ $m^2$ $s^{-1}$. Very high diffusivities also occurred in the model estimates for TS6, particularly for the general circulation model where mid-water column values exceeded 0.04 $m^2$ $s^{-1}$ (Supplemental Figure S9). The mixing simulation estimates were smaller but exceeded $10^{-2}$ $m^2$ $s^{-1}$ (Supplemental Figure S31). The high mixing brought the night time cooling throughout the water column for NN and MY (Supplemental Figures S28a-b); however, it homogenized the water column for LMD (Supplemental Figure S31c). LMD estimates for the vertical mixing parameterization were actually lower for TS6 than for NN or MY, since the weaker vertical stratification reduced the diffusivity. Generally, comparing the initial to the 20 day potential temperature and salinity transects of the general circulation model results in Supplemental Figures S3-S5 and S26-S28, the model replicates the general hydrography at 20 days, but tends to overmix the water column, particularly with the LMD vertical mixing parameterization. The ROMS model has been found to overmix in other simulations, with LMD mixing more than the other vertical mixing parameterizations [*Robertson and Hartlipp*, 2017; *Robertson and Dong*, 2019]. Nevertheless, despite the overmixing, the two layer structure persists on the east side and a well-mixed structure on the west side. Obviously, there is room for improvement in the vertical mixing parameterizations in ROMS.

Focusing on the mixing simulations and the mixing parameterizations, the model simulated the temperature structure of the water column other than the daily solar radiation in the upper layer during Time Series 4 reasonably well (Supplemental Figure S26). The temperature fields for all three mixing parameterizations were very similar (Supplemental Figure S26). Vertical temperature diffusivities were quite high in the upper layer, reaching $10^{-2}$ $m^2$ $s^{-1}$ and low in the lower layer, ~$10^{-6}$ $m^2$ $s^{-1}$, except near the bottom where values reached ~$10^{-4}$ $m^2$ $s^{-1}$ (Supplemental Figure S29a-b). The high diffusivities in the upper layer could have contributed to the heat from the daily solar cycle being quickly mixed throughout the upper layer and not being as evident. In contrast, the temperature fields were not well replicated at all for Time Series 5 (Supplemental Figure 27a-d). The vertical temperature diffusivities were much higher during this period, $10^{-4}$-$10^{-3}$ $m^2$ $s^{-1}$ throughout the water column (Supplemental Figure S30) and the water column became well mixed in the simulations. The winds were stronger and shifted directions during the first two days of Time Series 5 (Supplemental Figure S1c-d). Since wind mixing is one of the major factors in these simulations, higher mixing is expected with stronger winds. The temperatures in the simulations for Time Series 6 were similar to the observations, again without the daily solar cycle (Supplemental Figure S28a-d); however, the model responded more slowly and appears out of phase with the observations, possibly due to the lack of advection. After the first day, vertical temperature diffusivities were quite high, ~$10^{-2}$ $m^2$ $s^{-1}$ (Supplemental Figure S31). The winds during Time Series 6 were weaker and more consistent (Supplemental Figure S1e-f) than during Time Series 5. However, the stratification was quite weak during both Time Series 5 and 6, which will lead to higher diffusivity values from the model. For the conditions of these three Time Series, the model overmixes the water column regardless of the vertical mixing parameterization used. The overmixing by the model agrees with previous evaluations [*Robertson and Hartlipp*, 2017; *Robertson and Dong*, 2019].

## 5 Conclusions

In the shallow waters of the southern Arafura Sea near the Tiwi Islands, tides and the daily solar radiation cycle dominated the circulation in the form of tidal advection on the western side and internal tides on the eastern side. Slight changes in the topography resulted in the different dynamics between the eastern and western side of the Tiwi Islands. Extensive shallow water (< 30 m) regions exist on the western side compared to the eastern side. The daily solar radiation cycle on the western side increased the temperature, salinity, and density. The stratification as represented by the Brunt-Väsälä frequency increased due to the solar cycle and sank throughout the water column due to mixing, primarily by the wind. Cooler, fresher water occurred in deeper regions, especially in a trench. However, these waters were denser than the warmer, saltier water and did not flow in deep on the western side or were mixed with warmer water before they reached our sites. Tidal advection moved the entire water column past the time series sites, so alternating warmer, saltier and cooler, fresher water passed the site. The result was a barotropic situation on the western side. In the shallow water, evaporation increased the density more than the solar radiation decreased it. The eastern side was more baroclinic, with two clear layers separated at 20 m. The density of the lower layer was closer to that in the deeper water offshore as evidenced by a circulation simulation. Although there was a barotropic tide here too, it was weaker than on the eastern side and a baroclinic component was present with the two layers moving in opposite directions. Increases in the temperature due to surface radiation affected the entire water column, but upper 20 m were affected more and the increase in stratification was limited to the upper layer. The replenishment of the lower layer on the eastern side was reflected in an increase in fluorescence. Since fluorescence was limited to the lower water column on the eastern side but encompassed the entire water column on the western side, there are biological implications for these results.

## Acknowledgments and Data

We would like to thank Australia's Marine National Facility (MNF) and the crew of the RV Investigator for their assistance during this voyage. We would also like to thank our CTD operators and sampling team: Cristina Cerano Guerra, Rob Ryan, Cisco Navidad, Matthias Retsch, and Haydn Trounce. In many ways, they and the RV Investigator crew made this data set possible.

Funding for research was provided by an Internal Grant from Xiamen University Malaysia Research Fund XMUMRF/2018-C2/ICAM/0003 "Ocean Mixing in Various Conditions and its Handling in the Regional Ocean Modeling System (ROMS) Model" and grants from "Strategic Priority Research Program" of the Chinese Academy of Sciences No. XDB42000000 and the National Natural Science Foundation of China, 91858201 & 92058202 & 41721005. The funding for ship time was provided by MNF Grant IN2019_v06 "Maritime Continent observations of atmospheric convection, biogenic emissions, ocean vertical mixing, and the Indonesian Throughflow".

All the data from the voyage is available from the Australia Open Data Network (AODN) (https://portal.aodn.org.au/). The model simulation data are available upon request.

## References

Blauw, A. M., E. Nenica, R. E. P. M. Laane, N. Greenwood, J. Huisman (2012) Dancing with the tides: Fluctuations of coastal phytoplankton orchestrated by different oscillatory modes of the tidal cycle, *PLOS One*, 7(11), e49319, doi:10.1371/journal.pone.0049319.

Cloern, J. E. (1991) Tidal stirring and phytoplankton boom dynamics in an estuary, *J. Mar. Res*, 49, 203-221, doi:10.1357/002224091784968611.

Condie, S. A. (2011) Modeling seasonal circulation, upwelling and tidal mixing in the Arafura and Timor Seas, *Cont. Shelf Res*., 31, 1427-1436, doi:10.1016/j.csr.2011.06.005.

Easton, A. K. (1970) The tides of the continent of Australian, Horace Lamb Centre for Oceanographic Research, Flinders Univ. of South Australia, *Research Paper No. 37*, 1970.

Halpern, B. S., Wallbridge, S., Selkoa, K. A., Kappel, C. V., Micheli, F., D'Agrosa, C., et al. (2008) A global map of human impacts on marine ecosystems. Science, 319, 948-952, doi:10.1126/science.1149345.

Kampf, J. (2016) On the majestic seasonal upwelling system of the Arafura Sea, *J. of Geophys. Res*., 121, 12-18-1228, doi:10.1002/2015JC011197.

Locarnini, R. A., A. V. Mishonov, J. I. Antonov, T. P. Boyer, H. E. Garcia, O. K. Baranova, M. M. Zweng, C. R. Paver, J. R. Reagan, D. R. Johnson, M. Hamilton, and D. Seidov (2013), World Ocean Atlas 2013, Volume 1: Temperature. S. Levitus, Ed., A. Mishonov Technical Ed.; *NOAA Atlas NESDIS 73*, 40 pp.

Lozovatsky, I., Liu, Z., Wei, H., Fernando, H. J. S. (2008) Tides and mixing in the northwestern East China Sea Part 1: Rotating and reversing flows, *Cont. Shelf Res.,* 28, 318-337, doi:10.1016/j.csr.2007.08.006.

Moore, L. R., Huang, T. Ostrowski, M., Mazard, S., Kumar, S. S., Gamage, H. K. A. H., Brown, M. V., Messer, L. F., Seymour, J. R. Paulsen, I. T. (2019) Unicellular cyanobacteria are important components of phytoplankton communities in Australia's northern oceanic ecosystems, *Frontiers on Microbiology,* 9. 3356, doi: 10.3389/fmicb.2018.03356.

Pawlowicz, R., Beardsley, R., Lentz, S. (2002) Classical tidal harmonic analysis with error analysis in MATLAB using T-Tide, *Computers and Geoscience*, 28, 929-937, doi:10.1016/S0098-3004(02)00013-4

Robertson, R., C. M. Dong C. M. (2019) An evaluation of the performance of vertical mixing parameterizations for tidal mixing in the Regional Ocean Modeling System (ROMS), *Geoscience Letters*, 6 (15), doi:10.1186/s40562-019-0146-y.

Robertson, R., and P. Hartlipp (2017) Surface wind mixing in the Regional Ocean Modeling System (ROMS), *Geoscience Letters*, 4 (24), doi: 10.1186/s40562-017-0090-7.

Sharples, J. (2008) Potential impacts of the spring-neap tidal cycle on shelf sea primary production, *J. of Plankton Res*., 30 (2) 183-197, doi:10.1093/plankt/fbm088.

Shchepetkin, A., and J. C. McWilliams (2004) The regional oceanic modeling system (ROMS): a split-explicit, free-surface, topographic-following-coordinate oceanic model, *Ocean Modelling*, 9347-9404, doi:10/1016/j.ocemod.2004.08.002

Schiller, A, M. (2011) Ocean circulation on the North Australian Shelf, *Cont. Shelf Res.,* 31, 1082-2095, doi:10.1016/j.csr.2011.03.013.

Thurnherr, A. M. (2010) A practical assessment of uncertainties in full-depth velocity profiles obtained with Teledye/RDI Workhorse AcousticDoppler Current Profilers, *J. Atmos. Oceanic Technol*., 27, 1215–1227.

Whiteway, T.,G. (2009) Applying Geoscience to Australia's most important challenges, Record. *2009*/21. *Australian Bathymetry and Topography Grid.*

.